

An IMS–IMS Analogue of MS–MS

Stormy L. Koeniger,[†] Samuel I. Merenbloom,[†] Stephen J. Valentine,[‡] Martin F. Jarrold,[†] Harold R. Udseth,[§] Richard D. Smith,[§] and David E. Clemmer^{*,†}

Department of Chemistry, Indiana University, Bloomington, Indiana 47405, Predictive Physiology and Medicine (PPM), 1424 West Adams Hill, Bloomington, Indiana 47403, and Environmental Molecular Sciences Laboratory, Pacific Northwest National Laboratory, P.O. Box 999, Richland, Washington 99352

The development of a new ion mobility/mass spectrometry instrument that incorporates a multifold drift tube/ion funnel design is described. In this instrument, individual components from a mixture of ions can be resolved and selected on the basis of mobility differences prior to collisional activation inside the drift tube. The fragment ions that are produced can be dispersed again in a second ion mobility spectrometry (IMS) region prior to additional collisional activation and MS analysis. The result is an IMS–IMS analogue of MS–MS. Here, we describe the preliminary instrumental design and experimental approach. We illustrate the approach by examining the highly characterized bradykinin and ubiquitin systems. Mobility-resolved fragment ions of bradykinin show that b-type ions are readily discernible fragments, because they exist as two easily resolvable structural types. Current limitations and future directions are briefly discussed.

The measurement of an ion's mobility through a buffer gas has been used for a diverse range of applications, from chemical warfare agent detection to particle sizing¹ and is the basis of the technique referred to as ion mobility spectrometry (IMS).² A particularly attractive feature of IMS is that mobilities depend on molecular geometries such that it is often possible to resolve isomers or conformers that cannot be resolved by mass spectrometry.^{3–7} In addition, comparison of measured mobilities with values that are calculated for trial conformations (generated by quantum chemical and molecular modeling techniques) can provide structural information.⁸ This, combined with the rapid and sensitive

nature of the IMS measurement and soft ionization methods amendable to biopolymers,^{9–11} has led to the development of a number of IMS-based instruments. For example, several groups have now coupled IMS instruments to mass spectrometers^{1a,12} (MS and MS–MS) and liquid chromatography (LC) instruments¹³ to characterize complex biological mixtures.^{14–17}

Although significant effort to incorporate IMS with other methods to provide a multidimensional separation has been made, little work has been done to develop a multidimensional IMS separation. Several years ago, our group developed a simple split-

* To whom correspondence should be addressed. E-mail: clemmer@indiana.edu.

[†] Indiana University.

[‡] PPM.

[§] Pacific Northwest National Laboratory.

- (1) See, for example: (a) Creaser, C. S.; Griffiths, J. R.; Bramwell, C. J.; Noreen, S.; Hill, C. A.; Thomas, C. L. *P. Analyst* **2004**, *129*, 984–994. (b) Collins, D. C.; Lee, M. L. *Anal. Bioanal. Chem.* **2002**, *372*, 66–73. (c) Ewing, R. G.; Atkinson, D. A.; Eiceman, G. A.; Ewing, G. J. *Talanta* **2001**, *54*, 515–529. (d) Jarrold, M. F. *Annu. Rev. Phys. Chem.* **2000**, *51*, 179–207.
- (2) Mason, E. A.; McDaniel, E. W. *Transport Properties of Ions in Gases*; Wiley: New York, 1988.
- (3) Kim, S. H.; Spangler, G. E. *Anal. Chem.* **1985**, *57*, 567–569.
- (4) Von Helden, G.; Kemper, P. R.; Gotts, N. G.; Bowers, M. T. *Science* **1993**, *259*, 1300–1302.
- (5) Clemmer, D. E.; Hudgins, R. R.; Jarrold, M. F. *J. Am. Chem. Soc.* **1995**, *117*, 10141–10142.
- (6) Liu, Y.; Clemmer, D. E. *Anal. Chem.* **1997**, *69*, 2504–2509.
- (7) Counterman, A. E.; Valentine, S. J.; Srebalus, C. A.; Henderson, S. C.; Hoaglund, C. S.; Clemmer, D. E. *J. Am. Soc. Mass Spectrom.* **1998**, *9*, 743–759.

- (8) See, for example: Jarrold, M. F.; Constant, V. A. *Phys. Rev. Lett.* **1991**, *67*, 2994–2997. Mesleh, M. F.; Hunter, J. M.; Shvartsburg, A. A.; Schatz, G. C.; Jarrold, M. F. *J. Phys. Chem.* **1996**, *100*, 16082–16086. Shvartsburg, A. A.; Jarrold, M. F. *Chem. Phys. Lett.* **1996**, *261*, 86–91. Wyttenbach, T.; von Helden, G.; Batka, J. J., Jr.; Carlat, D.; Bowers, M. T. *J. Am. Soc. Mass Spectrom.* **1997**, *8*, 275–282. Barran, P. E.; Polfer, N. C.; Campopiano, D. J.; Clarke, D. J.; Langridge-Smith, P. R. R.; Langley, R. J.; Govan, J. R. W.; Maxwell, A.; Dorin, J. R.; Millar, R. P.; Bowers, M. T. *Int. J. Mass Spectrom.* **2005**, *240*, 273–284.
- (9) Fenn, J. B.; Mann, M.; Meng, C. K.; Wong, S. F.; Whitehouse, C. M. *Science* **1989**, *246*, 64–71.
- (10) Karas, M.; Bachmann, D.; Bahr, U.; Hillenkamp, F. *Int. J. Mass Spectrom. Ion Processes* **1987**, *78*, 53–68. Karas, M.; Hillenkamp, F. *Anal. Chem.* **1988**, *60*, 2299–2301.
- (11) Tanaka, K.; Waki, H.; Ido, Y.; Akita, S.; Yoshida, Y.; Yoshida, T. *Rapid Commun. Mass Spectrom.* **1988**, *2*, 151–153.
- (12) For IMS coupled to TOFMS, see: (a) Young, C. E.; Edelson, D.; Falconer, W. E. *J. Chem. Phys.* **1970**, *53*, 4295–4302. (b) Hoaglund, C. S.; Valentine, S. J.; Sporleder, C. R.; Reilly, J. P.; Clemmer, D. E. *Anal. Chem.* **1998**, *70*, 2236. (c) Gillig, K. J.; Ruotolo, B.; Stone, E. G.; Russell, D. H.; Fuhrer, K.; Gonin, M.; Schultz, A. J. *Anal. Chem.* **2000**, *72*, 3965–3971. (d) Thalassinou, K.; Slade, S. E.; Jennings, K. R.; Scrivens, J. H.; Giles, K.; Wildgoose, J.; Hoyes, J.; Bateman, R. H.; Bowers, M. T. *Int. J. Mass Spectrom.* **2004**, *236*, 55–63. (e) Clowers, B. H.; Dwivedi, P.; Steiner, W. E.; Bendiak Hill, B.; Hill, H. H. *J. Am. Soc. Mass Spectrom.* **2005**, *16*, 660–669. (f) Tang, K.; Shvartsburg, A. A.; Lee, H.; Prior, D. C.; Buschbach, M. A.; Li, F.; Tomachev, A.; Anderson, G. A.; Smith, R. D. *Anal. Chem.* **2005**, *77*, 3330–3339.
- (13) Valentine, S. J.; Kulchania, M.; Srebalus Barnes, C. A.; Clemmer, D. E. *Int. J. Mass Spectrom.* **2001**, *212*, 97–109. Venne, K.; Bonnell, E.; Eng, K.; Thibault, P. *Anal. Chem.* **2005**, *77*, 2176–2186. Li, J. J.; Purves, R. W.; Richards, J. C. *Anal. Chem.* **2004**, *76*, 4676–4683.
- (14) (a) Myung, S.; Lee, Y. L.; Moon, M. H.; Taraszka, J. A.; Sowell, R.; Koeniger, S. L.; Hilderbrand A. E.; Valentine, S. J.; Cherbas, L.; Cherbas, P.; Kaufmann, T. C.; Miller, D. F.; Mechref, Y.; Novotny, M. V.; Ewing, M.; Clemmer D. E. *Anal. Chem.* **2003**, *75*, 5137–5145. (b) Taraszka, J. A.; Kurulugama, R.; Sowell, R.; Valentine, S. J.; Koeniger, S. L.; Arnold, R. J.; Miller, D. F.; Kaufman, T. C.; Clemmer, D. E. *J. Proteome Res.* **2005**, *4*, 1223–1237. (c) Taraszka, J. A.; Gao, X.; Valentine, S. J.; Sowell, R. A.; Koeniger, S. L.; Miller, D. F.; Kaufman, T. C.; Clemmer, D. E. *J. Proteome Res.* **2005**, *4*, 1238–1247.
- (15) Moon, M. H.; Myung, S.; Plasencia, M.; Hilderbrand, A. E.; Clemmer, D. E. *J. Proteome Res.* **2003**, *2*, 589–597.
- (16) Liu, X.; Plasencia, M.; Ragg, S.; Valentine, S. J.; Clemmer, D. E. *Briefings Funct. Genomics Proteomics* **2004**, *3*, 177–186. Valentine, S. J.; Plasencia, M. D.; Liu, X.; Krishnan, M.; Naylor, S.; Udseth, H. R.; Smith, R. D.; Clemmer, D. E. *Nature Methods*, submitted.

field drift tube¹⁸ for ion mobility/mass spectrometry. In this instrument, mixtures of precursor ions are separated in a relatively long (~20 cm) low-field region, and immediately before exiting the drift tube for mass spectrometry (MS) analysis, the ions are exposed to a short (~1 cm) section that can be operated at low fields to pass the precursor ions or at high fields to generate fragment ions. By modulating the second region between the low- and high-field conditions, it is possible to obtain precursor and fragment ion mass spectra for mixtures of ions without initial mass selection, an approach that we referred to as a parallel method for analyzing a complex mixture.^{19,20} We subsequently used the approach to examine a number of complex protein mixtures, including tryptic digests of proteins extracted from the heads of the model *Drosophila melanogaster* organism,¹⁴ as well as digests of human plasma.¹⁶

In this paper, we describe the development of a new IMS instrument that extends the concepts of the split-field drift tube design.¹⁸ With this apparatus, it is possible to disperse a mixture of precursor ions on the basis of differences in mobilities and select an ion of specified mobility for collisional activation. The fragments, or new conformations, that are formed can then be separated again in a second low-field region before exposure to a second high-field region for activation and analysis by MS. This IMS–IMS approach is analogous in many ways to MS–MS strategies;²¹ however, the separations of the initial precursor and first dissociation products are based on cross section-to-charge (Ω/z) rather than mass-to-charge (m/z) ratios. Although the instrumentation is still at a preliminary stage of development, early results suggest that the ability to examine the mobility of fragment ions has substantial potential as a means of characterizing ion structure.

As described below, IMS–IMS takes advantage of the rapid progression of new instrument designs developed by us^{12b,18} as well as others.^{12f,22} In the past decade, many notable advances have been made. The instrumentation that is described below utilizes relatively long, low-pressure IMS regions (more than 2 m in some experiments). This design is facilitated by incorporating ion funnels²³ at strategic points along the drift region. These ion funnels serve several purposes, including a replacement for our other strategies^{14,24} for accumulating a concentrated pulse of ions

from the continuous electrospray ionization (ESI)⁹ source, a means of activating ions, and a method of refocusing diffuse ion clouds along the axis of the drift tube. Perhaps the most important feature of the IMS–funnel combination is the simplicity of design. As described below, the IMS–IMS experiments are conducted within a single tube, a simple design that should be straightforward to incorporate into many types of mass spectrometers (without significant loss of signal).

In this manuscript, we describe the IMS–IMS–MS instrument as well as the development of the ion funnel/drift tube assembly. We outline useful operational modes for IMS–IMS–MS and IMS–IMS (without MS analysis) experiments. We extend a previously proposed nomenclature^{12b} and symbolism^{21e,f} to describe the positions and generation of peaks within these new measurements. We illustrate these measurements by analyzing bradykinin^{25–30} and ubiquitin³¹ ions formed by ESI, systems that have been studied extensively. One significant aspect of this new technique is the ability to easily record mobility distributions for fragment ions. Currently, there are only a few reports involving the mobility of fragments.^{6,20,32} Here, we find that the b-type ions of bradykinin can be resolved into two types of conformations;³³ this allows these ions to be readily distinguished from other fragments in this system.

EXPERIMENTAL SECTION

Overview of Instrumentation. Figure 1 shows a schematic diagram of the ion mobility/time-of-flight instrument. Key to the present work is the incorporation of multiple ion funnels (F), drift

- (17) Synder, A. P.; Dworzanski, J. P.; Tripathi, A.; Maswadeh, W. M.; Wick, C. H. *Anal. Chem.* **2004**, *76*, 6492–6499. Jackson, S. N.; Wang, H. Y. J.; Woods, A. S. *J. Am. Soc. Mass Spectrom.* **2005**, *16*, 133–138. Dworzanski, J. P.; Tripathi, A.; Snyder, A. P.; Maswadeh, W. M.; Wick, C. H. *J. Anal. Appl. Pyrolysis* **2005**, *73*, 29–38. Ochoa, M. L.; Harrington, P. B. *Anal. Chem.* **2005**, *77*, 854–863.
- (18) Valentine, S. J.; Koeniger, S. L.; Clemmer, D. E. *Anal. Chem.* **2003**, *75*, 6202–6208.
- (19) Koeniger, S. L.; Valentine, S. J.; Myung, S.; Plasencia, M.; Lee, Y. L.; Clemmer, D. E. *J. Proteome Res.* **2005**, *4*, 25–35.
- (20) Hoaglund-Hyzer, C. S.; Li, J.; Clemmer, D. E. *Anal. Chem.* **2000**, *72*, 2737–2740.
- (21) See the following and references therein: (a) Kruger, T. L.; Litton, J. F.; Kondrat, R. W.; Cooks, R. G. *Anal. Chem.* **1976**, *48*, 2113–2119. (b) McLafferty, F. W.; Bockhoff, F. M. *Anal. Chem.* **1978**, *50*, 69–76. (c) McLafferty, F. W. *Acc. Chem. Res.* **1980**, *13*, 33–39. (d) Gross, M. L.; Chess, E. K.; Lyon, P. A.; Crow, F. W.; Evans, S.; Tudge, H. *Int. J. Mass Spectrom.* **1982**, *42*, 243–254. (e) Schwartz, J. C.; Wade, A. P.; Enke, C. G.; Cooks, R. G. *Anal. Chem.* **1990**, *62*, 1809–1818. (f) Schwartz, J. C.; Wade, A. P.; Enke, C. G.; Cooks, R. G. *Anal. Chem.* **1990**, *62*, 1809–1818. (g) Louris, J. N.; Broadbelt-Lustig, J. S.; Cooks, R. G.; Glish, G. L.; Vanberkel, G. J.; McLuckey, S. A. *Int. J. Mass Spectrom.* **1990**, *96*, 117–137.
- (22) Wyttenbach, T.; Kemper, P. R.; Bowers, M. T. *Int. J. Mass Spectrom.* **2001**, *212*, 13–23.

- (23) (a) Shaffer, S. A.; Tang, K. Q.; Anderson, G. A.; Prior, D. C.; Udseth, H. R.; Smith, R. D. *Rapid Commun. Mass Spectrom.* **1997**, *11*, 1813–1817. (b) Shaffer, S. A.; Prior, D. C.; Anderson, G. A.; Udseth, H. R.; Smith, R. D. *Anal. Chem.* **1998**, *70*, 4111–4119. (c) Shaffer, S. A.; Tolmachev, A.; Prior, D. C.; Anderson, G. A.; Udseth, H. R.; Smith, R. D. *Anal. Chem.* **1999**, *71*, 2957–2964. (d) Kim, T.; Tolmachev, A. V.; Harkewicz, R.; Prior, D. C.; Anderson, G.; Udseth, H. R.; Smith, R. D.; Bailey, T. H.; Rakov, S.; Futrell, J. H. *Anal. Chem.* **2000**, *72*, 2247–2255.
- (24) Hoaglund, C. S.; Valentine, S. J.; Clemmer, D. E. *Anal. Chem.* **1997**, *69*, 4156–4161. Henderson, S. C.; Valentine, S. J.; Counterman, A. E.; Clemmer, D. E. *Anal. Chem.* **1999**, *71*, 291–301.
- (25) Schnier, P. D.; Price, W. D.; Jockusch, R. A.; Williams, E. R. *J. Am. Chem. Soc.* **1996**, *118*, 7178–7189.
- (26) (a) Wyttenbach, T.; von Helden, G.; Bowers, M. T. *J. Am. Chem. Soc.* **1996**, *118*, 8355–8364. (b) Gill, A. C.; Jennings, K. R.; Wyttenbach, T.; Bowers, M. T. *Int. J. Mass Spectrom.* **2000**, *195*, 685–697. (c) Wyttenbach, T.; Kemper, P. R.; Bowers, M. T. *Int. J. Mass Spectrom.* **2001**, *212*, 13–23.
- (27) Freitas, M. A.; Marshall, A. G. *Int. J. Mass Spectrom.* **1999**, *183*, 221–231. Lifshitz, C. *Int. J. Mass Spectrom.* **2004**, *234*, 63–70.
- (28) Schneider, B. B.; Douglas, D. J.; Chen, D. D. Y. *J. Am. Chem. Soc. Mass Spectrom.* **2001**, *12*, 772–779. Mao, D. M.; Douglas, D. J. *Int. J. Mass Spectrom.* **2003**, *14*, 85–94.
- (29) Gimón-Kinsel, R. E.; Barbacci, D. C.; Russell, D. H. *J. Mass Spectrom.* **1999**, *34*, 124–136.
- (30) Purves, R. W.; Barnett, D. A.; Ells, B.; Guevremont, R. *Rapid Commun. Mass Spectrom.* **2001**, *15*, 1453–1456.
- (31) (a) Valentine, S. J.; Counterman, A. E.; Clemmer, D. E. *J. Am. Soc. Mass Spectrom.* **1997**, *8*, 954–961. (b) Li, J. W.; Taraszka, J. A.; Counterman, A. E.; Clemmer, D. E. *Int. J. Mass Spectrom.* **1999**, *187*, 37–47. (c) Purves, R. W.; Barnett, D. A.; Guevremont, R. *Int. J. Mass Spectrom.* **2000**, *197*, 163–177. (d) Reid, G. E.; Wu, J.; Chrisman, P. A.; Wells, J. M.; McLuckey, S. A. *Anal. Chem.* **2001**, *73*, 3274–3281. (e) Badman, E. R.; Hoaglund-Hyzer, C. S.; Clemmer, D. E. *J. Am. Soc. Mass Spectrom.* **2002**, *13*, 719–723. (f) Myung, S.; Badman, E.; Lee, Y. J.; Clemmer, D. E. *J. Phys. Chem. A* **2002**, *106*, 9976–9982. (g) Breuker, K.; Oh, H. B.; Horn, D. M.; Cerda, B. A.; McLafferty, F. W. *J. Am. Chem. Soc.* **2002**, *124*, 6407–6420. (h) Geller, O.; Lifshitz, C. *J. Phys. Chem. A* **2005**, *109*, 2217–2222.
- (32) Badman, E.; Myung, S.; Clemmer, D. E. *Anal. Chem.* **2002**, *74*, 4889–4894.
- (33) Counterman, A. E.; Clemmer, D. E. *Anal. Chem.* **2002**, *74*, 1946–1951.

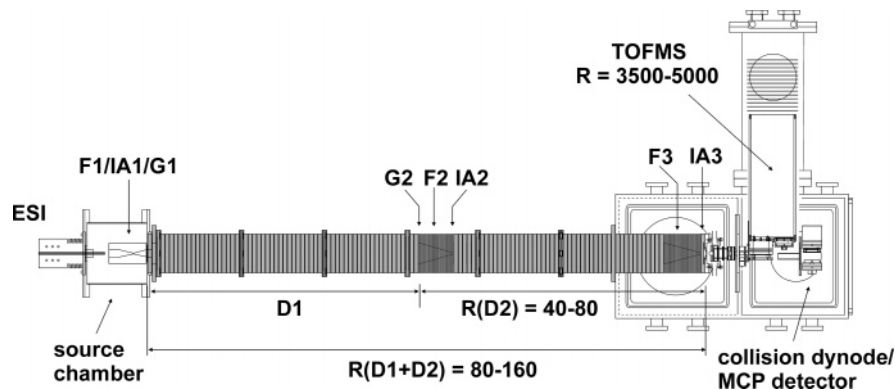


Figure 1. Schematic diagram of the ion mobility/time-of-flight instrument. The drift regions (D1 and D2), ion funnels (F1–F3), ion gates (G1 and G2), ion activation regions (IA1–IA3), and resolution (R) of specific components are labeled. Details of the instrument components are discussed in the text.

regions (D), and ion gates (G), as shown in the Figure.^{12f,26c} We refer to components in this instrument according to their location relative to the position at which ions are formed. F1 refers to the first funnel, used to focus and accumulate ions from a standard ESI source. Two other funnels, F2 and F3, are used to focus diffuse ion clouds. The combination of two drift regions (D1 and D2) and the funnels effectively creates an instrument that can be operated with one continuous or two discrete drift regions. The entire drift/funnel assembly is ~ 182 cm in length, and the assembly of lenses and spacers forms a cavity that can be filled with a buffer gas.

In addition to the drift regions and funnels, the instrument includes ion activation regions (IA). In the present configuration, IA1 is located immediately after F1; IA2 and IA3 follow F2 and F3, respectively. Ions exit the drift region into the first vacuum chamber ($\sim 8 \times 10^{-5}$ Torr), which houses standard ion focusing optics, and then into a second vacuum chamber ($\sim 8 \times 10^{-6}$ Torr), which houses an on-axis collision dynode/microchannel plate detection system for IMS–IMS measurements and an orthogonal geometry reflectron time-of-flight mass spectrometer (TOFMS) for IMS–IMS-MS measurements.

All electronics and data acquisition systems were designed in-house and are similar to components described elsewhere.^{12b} The system of drift tubes, funnels, and activation regions leads to four standard operational modes that are discussed in more detail below.

Description of Ion Funnel/Drift Tube Assembly. The ion funnel/drift tube assembly was developed through an iterative process that considered several other designs. Here, we briefly describe the geometry that appears to be most effective. The F1 funnel is housed in the source chamber and is used to focus and accumulate ions from the ion source, similar to a published design.^{12f} The ion funnel is operated using $50\text{--}70 V_{p-p}$, 450 kHz, and $11 V\cdot\text{cm}^{-1}$, with the last funnel lens held at a dc bias of 65 V relative to the applied drift voltage. Maximum transmission through F1 is obtained at high fields ($> 18 V\cdot\text{cm}^{-1}$); however, we observe higher trapping efficiencies at lower fields ($< 12 V\cdot\text{cm}^{-1}$). The F2 and F3 funnels are made of 31 (0.07-cm-thick) stainless steel electrodes (14-cm o.d.) with aperture diameters decreasing linearly from 7 to 0.56 cm spaced with 0.3-cm-thick Delrin spacers. For data presented here, F2 and F3 are operated at $100 V_{p-p}$ (480 kHz) and $70 V_{p-p}$ (450 kHz), respectively. Three RF generators

(built in-house) are used to supply the RF voltage to F1, F2, and F3. Electrical connections are made to F1 with ZIF sockets (3M, Austin, TX) mounted with printed circuit boards containing $1 M\Omega$ (0.1%) resistors in series that provide the dc field and 1000 pF (10%) capacitors in parallel that supply the RF voltage. F2 and F3 devices utilize $5\text{-}M\Omega$ (0.1%) resistors and 500-pF (10%) capacitors.

The two drift regions (D1 and D2) are constructed with modular drift tube sections that can be assembled in various lengths. The data shown below were recorded using D1 and D2 lengths of 87.1 and 94.9 cm, respectively, and drift fields of $12 V\cdot\text{cm}^{-1}$. Each section is composed of concentric stainless steel rings (14.0-cm o.d., 7.0-cm i.d.) that are isolated by 1.27-cm-thick Delrin spacers (14.0-cm o.d., 8.3-cm i.d.). The rings and spacers are stacked together, sealed with O-rings, and compressed using eight nylon threaded rods that run along the outside of the rings. Sections are joined together with a custom-made flange (15.3-cm o.d.) and a modified Delrin spacer to create the drift chamber that transmits ions from the source chamber into the main instrument chamber.

The dc fields across the drift tube and ion funnels are created with a continuous resistor chain ($5 M\Omega$, 1%) in series for D1, F2, D2, and F3, starting with a lens in the source chamber and terminating on a lens containing a grid located after F3. The exit region of the drift tube is described elsewhere.¹⁸ Several power supplies control the potential at desired points along this assembly. These points include the first and last drift lenses of D1 (both contain grids), the first and last lenses of D2 (both contain grids), and the lens after F3. The resistor chain is connected along the outside of the drift tube sections and ion funnels. The drift tube and ion funnel sections are filled with helium buffer gas to pressures of ~ 2.5 to 3.5 Torr.

Ion Gating for IMS–IMS and IMS–IMS-MS. Ion gating can be carried out at two points in the instrument shown in Figure 1. The first pulse on gate one (G1) is centered between the last funnel lens of F1 and the first lens of D1 (1.9 mm from each). The gate lens is constructed with a Ni mesh grid (90% transmittance, Buckbee-Mears, St. Paul, MN). Ions are trapped in the ion funnel with a bias of +85 V relative to the drift voltage and injected by dropping the bias to +15 V. The second gate is located between D1 and F2 and serves two functions: to mobility-select a specific peak from a previous mobility separation and to initiate the second mobility separation in D2. The pulse for G2 is generated by a

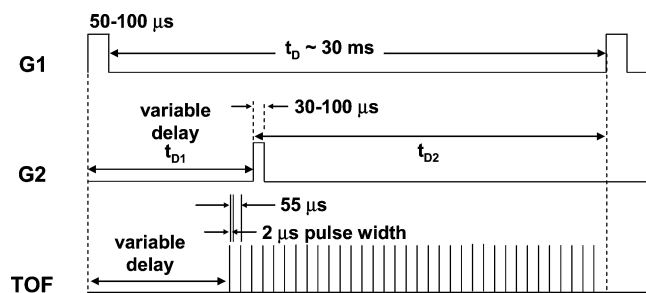


Figure 2. Pulse sequence for IMS–IMS and IMS–IMS–MS experiments. The pulse sequence labeled G1 is used to inject a pulse of ions into D1. This sequence is synchronized with the G2 and TOF sequences that are used for mobility selection and flight time acquisition, respectively. A typical set of values for pulse widths, repetition rates, and delay times are indicated.

pulse-delay generator (model DG535, Stanford Research Systems, Inc.) triggered by G1, as shown in the pulse sequence (Figure 2). The total drift times (t_D) of ions in the present instrument are a composite of the time spent in each region, which is ultimately defined by the fields and trajectories (path length). For the experiments presented here, the pulse sequence provides a direct measurement of ion drift times in D1 (t_{D1}) and D2 (t_{D2}), as indicated in Figure 2.

The ion gate of G2 is constructed with two grids, each on a 0.07-cm-thick stainless steel ring (14.0-cm o.d., 7.0-cm i.d.), spaced 0.3 cm apart with a Delrin spacer. This spacer is the same as those used in F2 and F3, allowing the ion gate to be compressed into an assembly that can be filled with the buffer gas (He in the experiments presented here; in other experiments, N₂ has been used). A power supply (Bertan, model 205B) controls the potential on the first lens, which defines the voltage at the end of D1. Ion gating is performed with the second lens, which is skipped in the resistor chain. The potential to this lens is supplied by an independent power supply set to maintain 14 V·cm⁻¹ for recording total mobility distributions and raised for ion gating (a dc bias of 20 V).

Ion Activation. Three independent regions in the instrument can be used for ion activation (labeled IA1–IA3 in Figure 1). The first region of ion activation (IA1) is in F1. Ion activation can be obtained here by changing the RF amplitude and dc field. The second region (IA2) is located between F2 and D2. Typically, RF is applied to the last lens of the funnel (in F2 and F3); however, this plate is operated with only a dc potential in F2 to create the second ion activation region (IA2). IA2 is created between this lens and the first lens of D2, which contains a grid to prevent RF fields from penetrating the second drift region. The voltages referred to in the data for ion activation in IA2 refer to the voltage drop across this region. The third region of ion activation (IA3) is located after F3 and is analogous to the split-field drift tube geometry published elsewhere.¹⁸

Ion Source Conditions. Positively charged ions of bradykinin (or ubiquitin) (Sigma 98% and 90% purity, respectively) are formed by electrospraying solutions containing 10⁻⁴–10⁻⁵ M peptide (or protein) in 49/49/2 (% volume) water/acetonitrile/acetic acid. ESI is performed with a pulled tip capillary at a solution flow rate of 0.25 μL·min⁻¹.

Modes of Operation. It is useful to describe the modes of operation for this system by presenting several hypothetical

datasets. Illustrations of data for four useful modes of operation for IMS–IMS and IMS–IMS–MS experiments are shown in Figure 3. We refer to these different acquisition scenarios as *operational modes A–D*. We note that the operations performed in these modes are with respect to the IMS dimension; therefore, these experiments can be performed with or without MS analysis.

Nomenclature Associated with IMS–IMS and IMS–IMS–MS Data. It is useful to describe the positions of peaks within nested IMS–MS datasets using the “drift (flight)” time [or $t_D(t_F)$] nomenclature that we described previously.^{12b} We note that any combination of units in the $t_D(t_F)$ nomenclature can be used [e.g., $t_D(m/z)$, $K(m/z)$ where K is defined as the mobility of the ion, etc.]. For the hypothetical data, we use $t_D(t_F)$ in units of ms and μs, respectively, and for the experimental data, we convert flight time values to a m/z scale and report $t_D(m/z)$. This system of nomenclature is sufficient for operational mode A (as discussed below); however, we find it useful to extend this system to describe peaks in other operational modes. In addition to the extended nomenclature, an extension of the symbolism proposed by Cooks and co-workers^{21e,f} that describes tandem MS experiments appears to be useful in describing these measurements. For tandem MS, a closed circle (●) denotes a fixed (or selected) mass, and an open circle (○), a variable (or scanned) mass. In an analogous fashion, tandem IMS (IMS–IMS) can be described by a closed square (■), and an open square (□), by a fixed mobility and a variable mobility, respectively. The transition between these measurements is described by an arrow (see Figure 3). For hybrid instruments, these symbols can be combined to describe the multidimensional measurements of IMS and MS. We demonstrate the extended nomenclature and symbolism by example for the following hypothetical data as well as the experimental data of bradykinin and ubiquitin.

Operational Mode A: Measurement of Traditional IMS and Nested IMS–TOF Distributions. The simplest mode of operating the instrument in Figure 1 involves acquisition of IMS and standard nested IMS–TOF data (operational mode A). Briefly, ions formed by ESI enter F1 through a conductance-limiting orifice, where they are accumulated (for ~20–200 ms) and then released in short pulses (from 50 to 100 μs) into D1. The release pulse activates the TOF pulser sequence as shown in Figure 2. As the ion mixture drifts through D1, individual components separate on the basis of differences in their mobilities. With no pulse applied to G2, all ions are transmitted into D2, where they continue separating. A key feature of the present design is the use of F2 and F3 funnels. As ions pass through these regions, they are radially focused. As described in more detail below, this reduces losses associated with diffusion and increases transmission. Ions that exit the drift tube are detected with the on-axis detector or focused into a TOF mass analyzer.

As shown in Figure 3a, the result of this operational mode is a conventional nested drift (flight) time dataset. This hypothetical case illustrates two pairs of isobaric ions (filled black) that can be identified from their $t_D(t_F)$ values (in ms and μs, respectively). For example, one pair of isobaric ions can be identified as 10.8–(22.5) and 11–(22.5). From the total drift times that are obtained from this experiment (and knowing the dimensions of the instrument), it is possible to determine the time that each ion spends in each region of the instrument. This time is used to

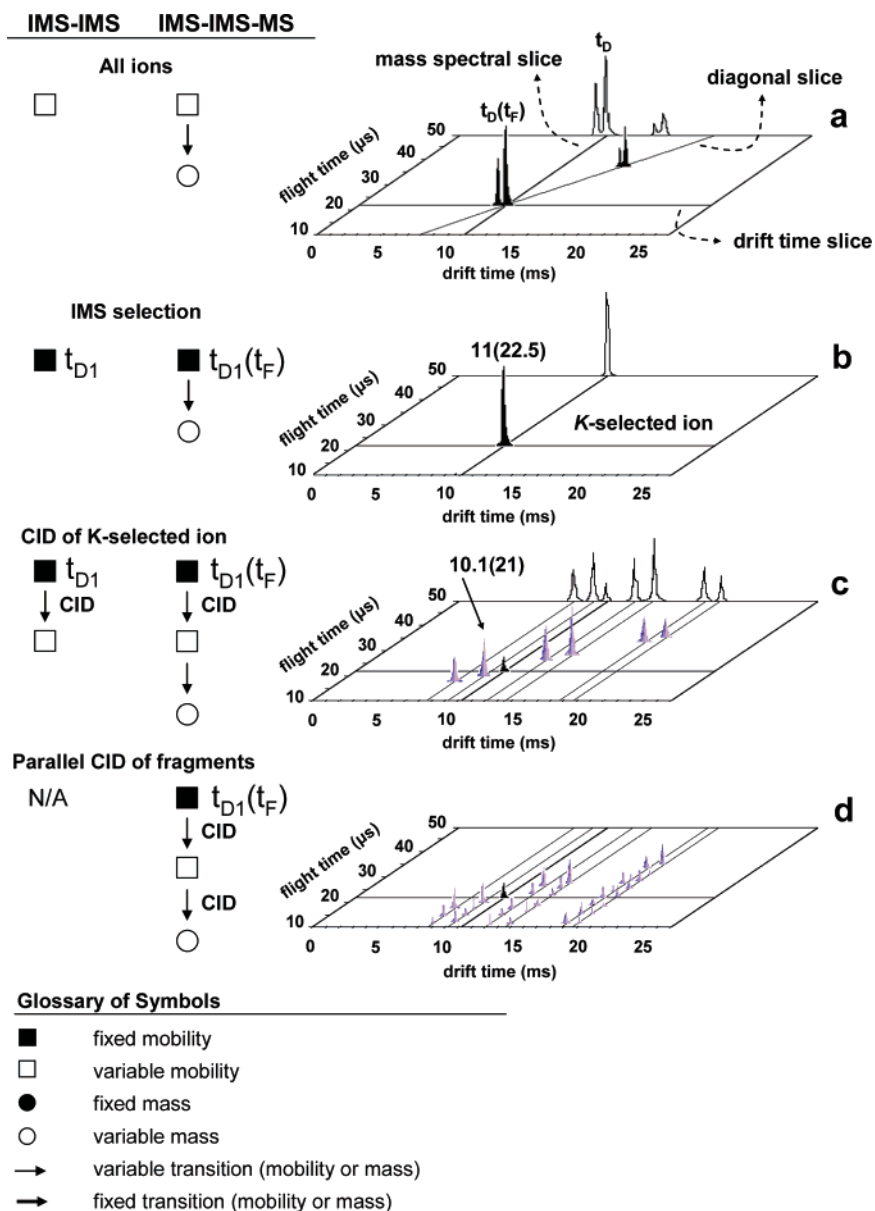


Figure 3. Four hypothetical distributions for several useful modes of operation. IMS–IMS–MS measurements are illustrated as nested $t_D(t_F)$ distributions, and ion mobility distributions (IMS–IMS) are shown as projections (solid line). The symbolism used to describe these operational modes is also shown. Distribution a, referred to as operational mode A, shows a standard nested $t_D(t_F)$ dataset. Specific extractions of data from $t_D(t_F)$ distributions are labeled. Distribution b shows the isolation of one peak, referred to as operational mode B. Distribution c shows the distribution of mobility-separated, primary fragments that is obtained when the mobility-selected ions are exposed to energizing collisions at IA2, referred to as operational mode C. Distribution d shows a spectrum in which the mobility-separated, primary fragments are exposed to energizing collisions at the exit of the drift tube to produce secondary fragment ions, referred to as operational mode D. See text for details.

determine the delay time associated with ion selection (t_{D1} in ms) and can also be used to calculate collision cross sections for precursor ions.

The symbolism used to describe operational modes A–D for IMS–IMS(–MS) is also shown in Figure 3. We note that data obtained by integration of all drift or flight time values represents a one-dimensional measurement that can be denoted by a circle or square, respectively; however, data extracted over a narrow range within the dataset (as shown in Figure 3a) do not necessarily represent the physical measurement and are, therefore, denoted by the symbolism of the original measurement.

Operational Mode B: Selection of a Narrow Distribution of Mobilities. By applying a synchronized delay pulse to G2, as

shown in the pulse sequence in Figure 2, it is possible to transmit only ions with a specific mobility into the D2 region, as shown in Figure 3b. When only a single stable structure (or narrow range of stable structures having identical K values) is present, the resultant $t_D(t_F)$ distribution will contain only the single narrow peak that was selected; however, if more than one component is present during the selection, these may undergo additional separation in D2. In contrast, a distribution of unstable K -selected structures (i.e., structures that are interconverting on the timescales of the measurement) may appear as a broad peak. Figure 3b illustrates the former case.

For operational mode B–D, we specify the selected ion by the selection time that is used [t_{D1} for IMS–IMS or $t_{D1}(t_F)$ for

IMS–IMS-MS], followed by an arrow. For example, the selected ion observed in operational mode B in Figure 3b for IMS–IMS-MS would be denoted as $t_{D1}(t_F) \rightarrow t_D(t_F)$ or 5.27(22.5) \rightarrow 11(22.5), where t_F corresponds to the value for the K -selected ion as well as the species that is detected (since in this operation mode, no dissociation is employed). For IMS–IMS, this would be denoted as $t_{D1} \rightarrow t_D$.

Operational Mode C: Activation of K -Selected Ions. It is possible to induce structural changes or dissociation of K -selected ions inside the drift tube and then separate the different structures or fragments in D2. Figure 3c shows a hypothetical distribution illustrating the separation of fragment ions (shaded peaks) that were produced at IA2. Fragments may have mobilities that are less than or greater than the antecedent precursor ion mobility. Fragments having mobilities that are greater than the precursor will exit the drift tube before the precursor [i.e., 5.27(22.5) \rightarrow 10.1(21)], whereas fragments with lower mobilities will have drift times that are longer than the precursor [i.e., 5.27(22.5) \rightarrow 14.5(30)]. In both cases, fragments are easily discernible in IMS–IMS-MS measurements because, in addition to shifts in mobility, they have different m/z values.

In this case, the i fragment ion peaks that arise from fragmentation of a selected ion ($t_{D1}(t_F) \rightarrow$) would be designated as $t_{D1}(t_F) \rightarrow t_D(t_F)_i$, as demonstrated above. We note that in this case, the total drift time associated with a fragment ion peak will be the composite of the selected ion drift time (t_{D1}) and the time associated with the migration of the fragment through the remaining portion of the drift tube.

Operational Mode D: Parallel Dissociation of Fragment Ions That Were Formed from Mobility-Selected Precursors. Figure 3d shows a mode in which additional fragmentation is introduced at IA3. In this example, a K -selected distribution has been activated at IA2, and the fragments that are formed are separated in D2 prior to activation at IA3. In the product ion distribution, it is possible to correlate secondary fragment ions with the primary fragment from which they arose, because primary and secondary fragments have coincident drift times. This experiment has analogies with mass spectrometry based MS³ analyses. That is, it is possible to resolve (and identify) secondary fragment ions that were formed from an initially mobility-defined precursor (and primary fragment). We note that this mode of operation is useful only for IMS–IMS-MS experiments.

By extension, the positions of peaks produced in operational mode D, in which the fragmentation of each of the separated $t_D(t_F)_i$ primary fragment ions produces j secondary fragments, would be denoted as $t_{D1}(t_F) \rightarrow t_D(t_F)_i \rightarrow t_D(t_F)_j$ or 5.27(22.5) \rightarrow 10.1(21) \rightarrow 10.1(12.5) for the lowest m/z fragment of this primary ion shown in Figure 3d. The present nomenclature can be extended to describe pathways of structural changes (such as folding and unfolding transitions in protein ions that are introduced by collisional activation) that do not involve fragmentation.

RESULTS AND DISCUSSION

Development of a Hybrid Ion Funnel/Drift Tube Instrument. A primary motivation for the incorporation of ion funnels with drift regions is associated with improving ion transmission. As ions separate through the body of the drift tube, they undergo diffusion such that the size of the ion cloud at the exit of the drift tube may be much larger than the exit aperture. The ion funnel

allows for radial focusing of the ions, facilitating high transmission through small apertures, even for extended drift regions.^{12f} Initially, we were concerned that ion focusing in the funnel might influence the ability to resolve peaks, and some experimental settings lead to a loss of resolution; however, other settings allow high-resolution measurements to be made. Empirically, we find that when the dc field in the funnel is at or above the field used in the drift regions, high-resolution mobility separations can be obtained. When the dc field in the funnel is below the drift field, resolution is lost. The loss in resolution is dependent on the mobility of the ion. An explanation for this is provided from theoretical simulations of the funnel/drift tube interface, discussed in more detail below.

Ion Transmission. One means of assessing transmission is to examine the ion signals associated with well studied systems. In previous reports, we have presented detailed studies of the detection limits of nested $t_D(t_F)$ measurements for standard peptides, such as bradykinin, angiotensin I and II, and others (over a range of concentrations). In these systems, detection limits for nested $t_D(t_F)$ measurements in the range of \sim 100 amol to \sim 1 fmol are typical (at a signal-to-noise ratio of 3:1).^{14a} From similar measurements of these systems, we estimate that our transmission efficiency in the hybrid drift tube/funnel instrument is about a factor of 4 below the efficiency that is obtained for short, simple designs, ranging from \sim 0.4 to 4 fmol for these peptides. At the current stage of development, the detection limit is most likely limited by the trapping efficiency associated with F1, which typically ranges from \sim 8 to 20%. Studies of K -selected ion signals indicate that selection can be accomplished with little or no loss of the selected species.

Simulations of Ion Trajectories in the Drift Tube/Funnel Interface Region. Figure 4 shows ion trajectory simulations at the D1–F2–D2 interface region. Trajectories are calculated using an algorithm written in-house that is conceptually identical to other algorithms.²³ A brief description is as follows: The calculations utilize a three-dimensional field array created in SIMION³⁴ to determine ion displacements over short time increments. For such calculations, the displacement of an ion is the sum of the ion motion contributions from the mobility (K) as well as the diffusion of the ion. The former contribution is field-dependent (i.e., the drift velocity is proportional to the product of the mobility and the electric field),² whereas the latter is a random contribution in the algorithm (discussed below).

The modeling of RF fields for the ion funnel requires the use of two field arrays created in SIMION.³⁴ One array contains all field values associated with each grid unit under conditions in which one set of ion funnel lenses (those capacitively coupled; see above) is at the maximum peak RF voltage and the other set of ion funnel lenses is at the minimum peak voltage; the second array is defined with inverse peak RF voltages. Initially, the algorithm reads in regions of both arrays flanking the three-dimensional positions of ions. The x , y , and z -dimension fields at time t are then calculated for the eight points immediately surrounding the ion. The calculation is accomplished by adding the time-dependent RF field to the dc field for each of the eight points [i.e., $(E_{RF} + E_{dc})_x$, $(E_{RF} + E_{dc})_y$, $(E_{RF} + E_{dc})_z$]. The RF fields

(34) Dahl, D. A. SIMION (Version 7.0); Idaho National Engineering Laboratory: Idaho Falls, ID.

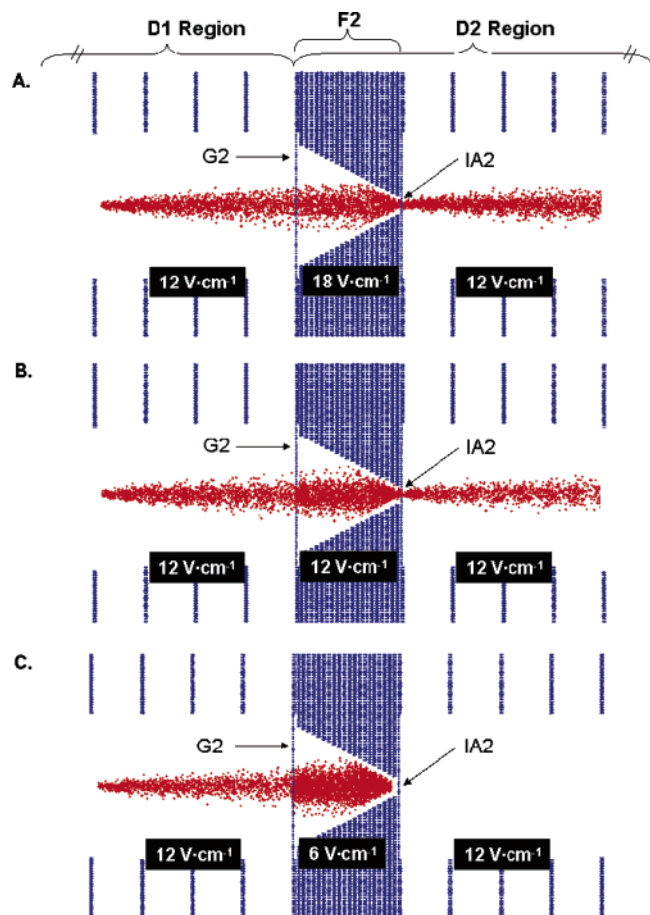


Figure 4. Cross-sectional view of the instrumental diagram for the D1–F2–D2 lens system interface (blue) and trajectory simulations (red) for 200 ions that are calculated using the mobility for singly charged bradykinin under the experimental conditions described in the text. The simulations were carried out using $12 \text{ V}\cdot\text{cm}^{-1}$ for each of the drift regions while three ion funnel fields were investigated (18 , 12 , and $6 \text{ V}\cdot\text{cm}^{-1}$ for simulations A, B, and C, respectively). A frequency of 450 kHz was utilized for all trajectory calculations. The red dots show a composite of different positions that are observed for the distribution of 200 ions at ~ 100 different time steps across the simulation. See text for details.

are obtained by multiplying the peak field (that corresponds to settings where the funnel lenses are at the RF peak voltages) by the sine of the angular frequency multiplied by the total drift time [for each dimension, $E_{\text{RF}} = E_{\text{RF(peak)}} \sin(\omega t_{\text{D}})$]. The angular frequency is obtained from the user-defined RF frequency (450 kHz in Figure 4). The calculated fields are then used to determine ion displacement in each dimension resulting from the mobility as described above.

Ion diffusion coefficients are obtained from eq 1.²

$$D = \frac{k_{\text{B}}TK}{e} \quad (1)$$

Here, the variables k_{B} , T , and e correspond with Boltzmann's constant, temperature, and the charge of the ion, respectively. For ions used in the simulations, K is obtained from experiments (e.g., the mobilities of different charge states of bradykinin⁷ as well as the elongated conformer of the $+7$ charge state of

ubiquitin^{31a}). The algorithm simulates the displacement of ions due to diffusion using eq 2.²

$$\sqrt{\langle r^2 \rangle} = (6D\Delta t)^{0.5} \quad (2)$$

Here, $\sqrt{\langle r^2 \rangle}$ is the root-mean-square displacement of the ion for time increment Δt . To simulate random diffusion in three dimensions, $\sqrt{\langle r^2 \rangle}$ is converted into a polar coordinate vector by randomizing azimuth and elevation angles for each calculation. The resultant vector is then dissected into its constituent x , y , and z vectors from a square root of the sum of the squares calculation using the given angles. Such values are added to those resulting from the three-dimensional mobility calculations to provide an overall ion displacement for each time increment.

Two-dimensional examples of trajectory calculations for three different D1–F2–D2 conditions are shown in Figure 4. Each has been examined in some detail by monitoring ion signals as experimental parameters are varied. In general, these simulations show that as ions travel through the drift tube, they diffuse into a sizable cloud (in the D1 region); as they pass through F2, the diffused cloud collapses such that ions are efficiently transmitted into the second-mobility region (D2). As ions travel through D2, the absence of the RF from the ion funnel no longer constrains the ions radially, and the ion packet diffuses again. Similar simulations of F3 show that ions can be focused through the IMS-MS interface.

Over the course of these simulations, we examined a number of different funnel geometries, lens spacings, RF frequencies, and magnitudes for a range of mobilities (corresponding to ions of known cross section and charge state). We focused most of our effort on ions with $K = 0.06\text{--}0.17 \text{ m}^2\cdot\text{s}^{-1}\cdot\text{V}^{-1}$. Our calculations suggest that one useful design involves funnel lens spacing of 0.3 cm (or below) operated in the $300\text{--}500 \text{ kHz}$ range using $50\text{--}100 \text{ V}_{\text{p-p}}$.

These simulations provide some insight about the empirically derived operation parameters for the D1–F2–D2 region (described above). It appears that in this region, a key factor in this combination of devices is the ratio of the dc fields used in the drift and funnel regions. When the dc component of the F2 region is at or above the fields employed for D1 and D2, the simulations show that it is possible to transmit $\sim 100\%$ of the ions. Alternatively, if the dc component of F2 is below a critical value (cf., the 12 and $6 \text{ V}\cdot\text{cm}^{-1}$ examples in Figure 4), ions become increasingly trapped in the funnel. Experimentally, we observe a significant decrease in the measured ion signal that is transmitted when using such experimental settings. We note that Figure 4 shows no ion transmission for the mobility of the ion simulated; however, higher mobility ions could still be transmitted under these conditions. This result also provides some insight about the origin of resolution loss: as two mobility-resolved ion clouds pass through a region where they are trapped (or near the threshold for trapping), they will be temporally broadened (resulting in a loss of resolution).

One final comment involving these simulations is that they suggest modes of operation that we have not examined experimentally (yet). For example, combined with a gate that is located before the funnel, the ability to trap ions in F2 makes it possible

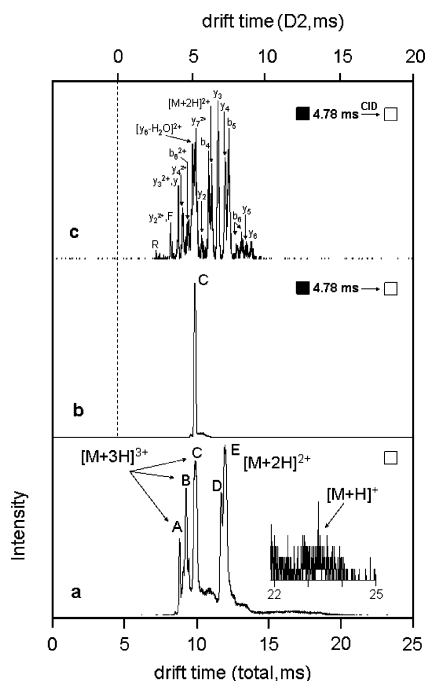


Figure 5. IMS–IMS drift time distributions of electro sprayed bradykinin ions shown on two time scales: the total drift time (bottom) and the drift time observed after mobility selection (t_{D2}), that is shifted by the selection time (as indicated by the dashed vertical line). Part a shows the distribution for all ions and includes an inset to show the low-intensity feature that is often associated with $[M_n + nH]^{n+}$ ions. Part b shows the feature labeled C after it has been selected at G2 (see Figure 2). Part c shows the distribution of fragment ions that are observed when C is activated at IA2 using 126 V.

to accumulate mobility-selected ions from multiple initial ion packets. In this case, a short D1 region in which mobility-selected ions are accumulated from many injection pulses from the source, followed by a much longer D2 region, would improve the duty cycle of selected ion–IMS experiments. The duty cycle improve-

ment should scale as the ratio of the D2/D1 lengths (or D1/D2 fields).

IMS–IMS Measurements of Bradykinin. Much of the experimental work has involved understanding how to select and collisionally activate a specific species. These experiments are simplified by bypassing the MS analysis. Figure 5 shows several ion mobility distributions for bradykinin ions produced by ESI that demonstrate IMS–IMS. These distributions were recorded using the on-axis detector. The ion mobility distribution obtained without selection or activation shows several resolved peaks at drift times of 8.95, 9.30, 10.07 ms and a peak that is partially resolved at 12.12 ms. In separate experiments (shown below) we measured the m/z values for each of these features, making it possible to assign the three resolved peaks as $[M + 3H]^{3+}$ ions and the partially resolved features as $[M + 2H]^{2+}$ ions. From the total drift times (and operation conditions), we determine the approximate delay time ($t_{D1} = 4.78$ ms) required to select one of the $[M + 3H]^{3+}$ peaks. The approximate selection time can be determined on the basis of the ratio of the fields of D1 and D2. Selection of this peak (operational mode B) is shown in Figure 5b. When the IA2 region is set to fragmentation conditions, this selected ion is activated, and new fragments are formed as shown in Figure 5c (operational mode C). It is interesting that this type of experiment gives a very detailed fingerprint of this molecule (even without MS analysis), suggesting that such an IMS–IMS approach should be useful for IMS-only devices as a means of improving selectivity.

Nested IMS–IMS-MS Measurements of Bradykinin. Figure 6 illustrates operational mode A. This nested $t_D(m/z)$ distribution shows evidence for many features that we have observed previously. For example, we observe the singly protonated monomer $[M + H]^+$ at 23.50(1061.2) as well as the $[M_2 + 2H]^{2+}$ [18.43(1061.2), 18.79(1061.2)] and $[M_3 + 3H]^{3+}$ [16.78(1061.2)] multiply charged multimers. This distribution is very reproducible (i.e., for any two measurements, the positions of resolved peaks

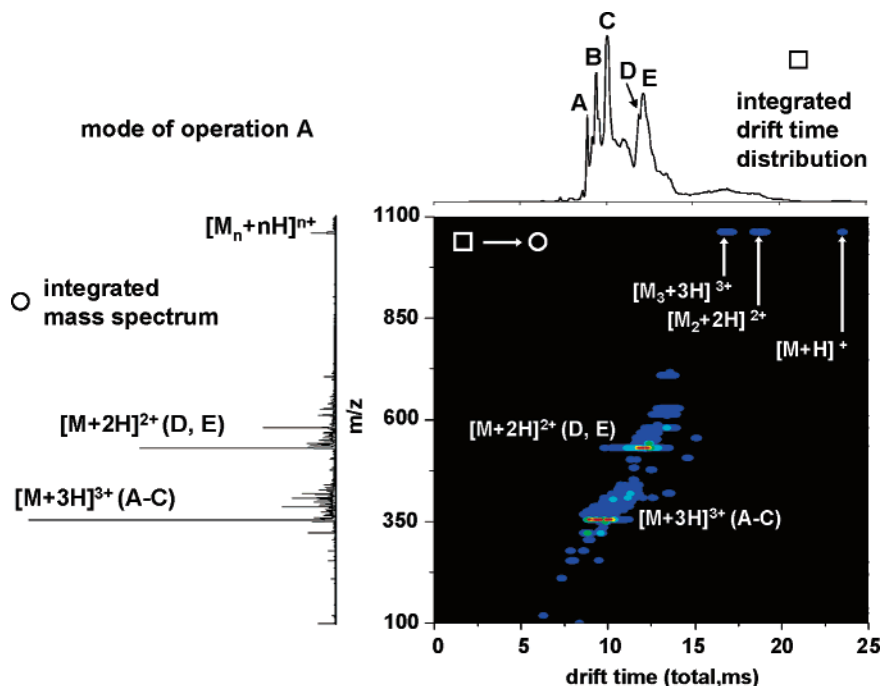


Figure 6. Nested $t_D(m/z)$ dataset obtained for electro sprayed bradykinin using operational mode A. See text for details.

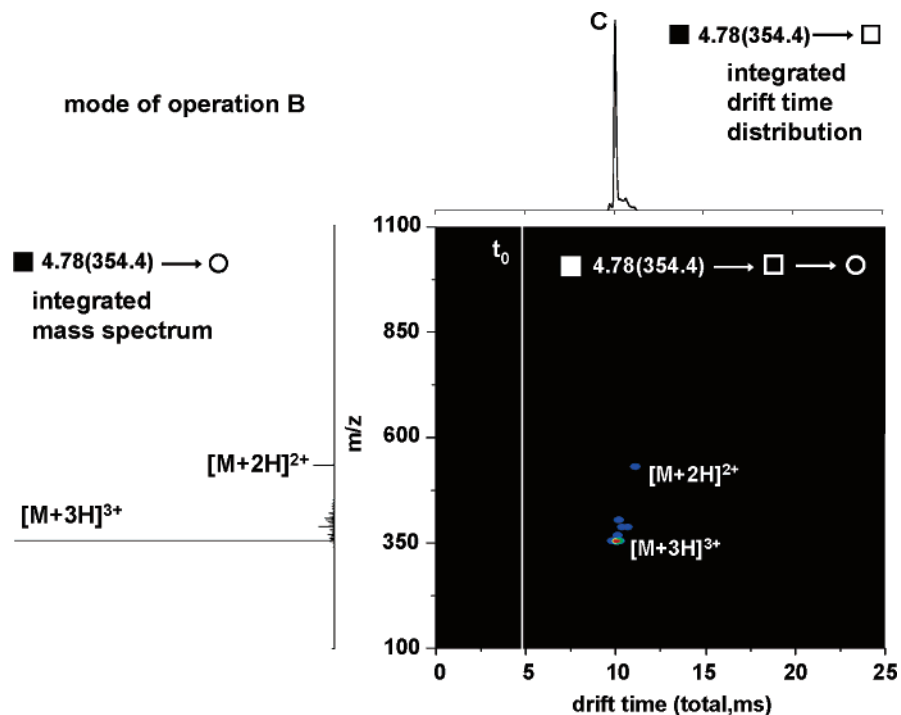


Figure 7. A nested $t_D(m/z)$ distribution for bradykinin using operational mode B showing the selection of a peak at G2 using a delay time of $t_{D1} = 4.78$ ms (50- μ s pulse width). Also indicated is the t_0 (vertical white line) for the mobility separation in D2. See text for details.

typically agree to within 1% (relative uncertainty); the intensities for a defined set of conditions over the period of hours are usually within $\pm 10\%$. Close inspection shows features that are somewhat different in appearance from data that we^{12d} and others²⁶ have published previously for bradykinin. The primary difference is associated with the large increase in signal associated with the $[M + 3H]^{3+}$ ion which exists as three resolved features. Only a single sharp peak was observed previously for this ion. At this point, we do not fully understand why additional $[M + 3H]^{3+}$ structures are observed; however, we note that the ion source configuration used here is very different from any we have used before. We note also that this source appears to favor higher charge states, and the relative intensity of the mass spectral peak for the $[M + 3H]^{3+}$ ion is substantially increased relative to our other sources.

Experimental Data Demonstrating Ion Selection and Selected Ion Dissociation (Operational Modes B and C). Figure 7 shows the distribution obtained in operational mode B. In this case, a 50- μ s window delayed 4.78 ms with respect to the initial pulse was used to select one of the resolved $[M + 3H]^{3+}$ ions. The resulting distribution shows that the 4.78(354.4) \rightarrow 10.07(354.4) peak dominates the distribution. A smaller 4.78(354.4) \rightarrow 11.13(531.1) peak is also observed. The decrease in mobility along with the change in m/z show this is the formation of some $[M + 2H]^{2+}$.

Proton transfer (with He) is expected to be highly endothermic for $[M + 3H]^{3+}$; it is possible that some proton transfer occurs with residual solvent vapor inside the drift tube.³⁵ The observation of this process indicates that some ion activation occurs post selection. In addition to being shifted in m/z , the $[M + 2H]^{2+}$ peak also has a different drift time. Because the cross section for this ion is known (and cross sections can be obtained from D2

through a calibration), the point at which the proton-transfer reaction occurred can be located; in this case, the 4.78(354.4) \rightarrow 11.13(531.1) peak must have been generated at IA2 (not F2, D2, F3 or IA3). Thus, even under relatively mild conditions, some activation has occurred. There is also evidence for some very weak features (in the $m/z = 360\text{--}400$ range) that appear to have been formed in the IA2 region.

Figure 8 shows a distribution of mobility-separated, fragment ions produced when an IA2 bias of 126 V is employed. The new distribution shows a number of large peaks. Some of these (e.g., 4.78(354.4) \rightarrow 8.24(119.9), 4.78(354.4) \rightarrow 9.07(253.8), and 4.78(354.4) \rightarrow 9.48(321.7)) have total drift times that are less than the $[M + 3H]^{3+}$ precursor, indicating that the mobilities of these ions are higher than that for $[M + 3H]^{3+}$. Others (e.g., 4.78(354.4) \rightarrow 11.18(408.5), 4.78(354.4) \rightarrow 11.60(419.5), 4.78(354.4) \rightarrow 12.07(506.6), 4.78(354.4) \rightarrow 12.89(642.3), and 4.78(354.4) \rightarrow 14.49(807.5)) have lower mobilities than $[M + 3H]^{3+}$. For this known system, it is possible to assign essentially every feature that is observed in Figure 8.

It is instructive to examine mass spectra under different IA2 conditions. Figure 9 shows integrated mass spectra (and gives assignments) for several different conditions that have been used to activate the $[M + 2H]^{2+}$ and $[M + 3H]^{3+}$ ions. In general, higher-charge-state ions can be activated at lower IA2 voltages, a result that can be explained by increased rates of dissociation due to the larger coulomb force, which destabilizes the precursor.^{25,36} The degree of fragmentation can be tuned over a substantial range

(35) The proton affinity of He is 42.5 kcal/mol, as given by: Lias, S. G.; Bartmess, J. E.; Liebman, J. F.; Holmes, J. L.; Levin, R. D.; Mallard, W. G. *J. Phys. Chem. Ref Data* **1988**, *14* (Suppl. 1), 1. We have previously observed proton transfer upon high-energy injection into drift tubes containing high-purity He; it is possible that some residual water vapor also contributes to this process.

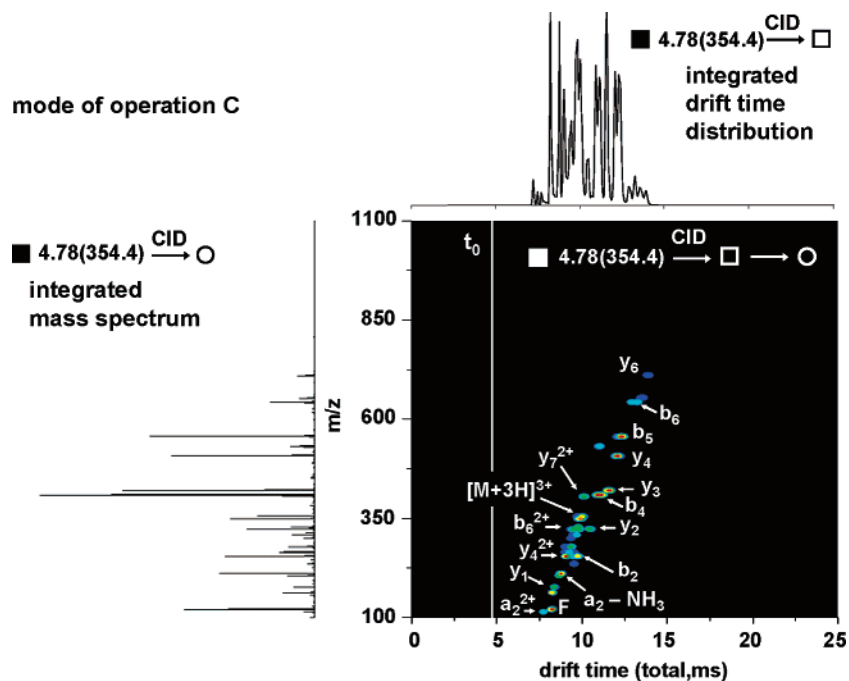


Figure 8. A nested $t_D(m/z)$ distribution for bradykinin obtained using operational mode C. Fragmentation is achieved by applying 126 V at IA2. The mobility-separated fragment ions corresponding to the b- and y-ion series are labeled. See text for details.

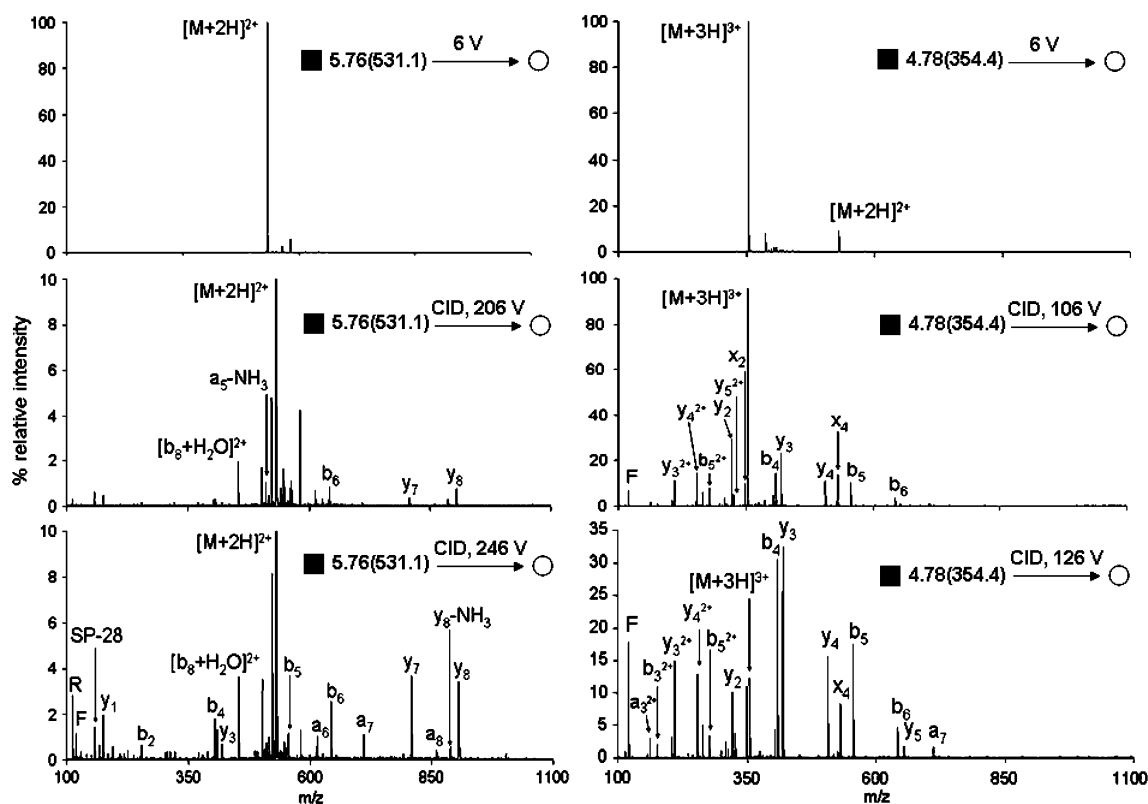


Figure 9. Mass spectra obtained by integration across all drift times for all precursor and fragment ions produced in operational mode C are shown for the selection and activation of peak E [12.12(531.1)] (left) and peak C [10.07(354.4)] (right). Refer to Figure 6 for assignments of peaks in the parent ion distribution. Peak E was selected at $t_{D1} = 5.76$ ms (60 μ s), and peak C was selected at $t_{D1} = 4.78$ ms (50 μ s). As in Figure 8, the fragment ions in the mass spectra are separated in mobility through D2.

(from minimal fragmentation at ~ 6 V to extensive fragmentation at ~ 246 V). Although we do not show data here, IA2 activation

(36) Rockwood, A. L.; Busman, M.; Smith, R. D. *Int. J. Mass Spectrom. Ion Processes* **1991**, *111*, 103–129. Ishikawa, K.; Nishimura, T.; Koga, Y.; Niwa, Y. *Rapid Commun. Mass Spectrom.* **1994**, *8*, 933–938.

has been used to produce fragments of several proteins as well as oligosaccharides.³⁷ Thus, it is a general approach that should be useful for many different types of ions. For a specific set of conditions, fragmentation patterns are highly reproducible.

(37) Koeniger, S. L.; Merenbloom, S. I.; Clemmer, D. E. Work in progress.

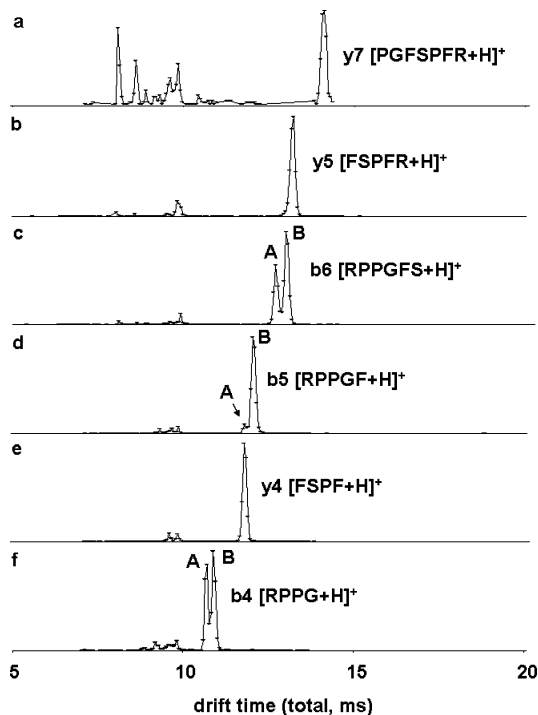


Figure 10. Ion mobility distributions of several b- and y-ions formed by selection [$t_{D1} = 4.78$ ms ($50 \mu\text{s}$)] and dissociation of peak C [10.07-(354.4)] in IA2 with 126 V. Drift time slices are obtained from the nested $t_D(t_F)$ dataset in Figure 8 by integrating drift times for a narrow range of m/z values. The b-ion series exhibits two conformations, labeled A and B, corresponding to a compact and elongated structure, whereas the y-ion series exhibits a single peak (see text for discussion).

It is also interesting to examine the ion mobility distributions for fragment ions. Although ion mobility data for literally thousands of peptides have been measured,³⁸ so far, there is very little information about the structures of fragment ions.^{6,12b,20,32} Arguably, information about fragment ion mobilities (and structures) are of interest for a number of fundamental reasons (e.g., understanding dissociation mechanisms) as well as applied uses (fragment ion mobilities provide additional constraints for assignment). Figure 10 shows drift time slices for six fragment ions (either b- or y-type). The distributions for y-type ions show a single sharp peak, whereas each of the b-type fragments shows evidence for two peaks. The latter fragments must exist as at least two different conformations, and it will be interesting to apply modeling to investigate the structural differences. We note that within experimental uncertainty (about $\pm 10\%$), the ratio of these two resolved peaks (for a single m/z ion) appears to be the same, regardless of how they are produced (i.e., the distributions appear to be similar at different IA2 activation voltages, and the same distributions are obtained when fragmentation is initiated from $[M + 2H]^{2+}$ precursors). This suggests that the structures and populations are not influenced by how the dissociation transition state is approached; rather, the distribution appears to stabilize both populations after dissociation.

Finally, although these results pertain to only a single system, we cannot help but note that the results are provocative. If the

peak differences associated with b- and y-type ions (or other ions) are intrinsic to these fragments, then the mobility dimension would offer a complementary means to assign mass spectral peaks to specific types of ions. That is, in the case of bradykinin, the doublet is indicative of a specific fragment type (b-ions). Clearly, this mobility signature may be different for other peptide sequences (and precursor ion charge states); however, the ability to distinguish a specific ion type from its mobility (or peak appearance) could greatly facilitate the use of fragmentation data for de novo sequencing.³⁹ We are currently investigating the fragmentation distributions that are obtained for other types of sequences and charge states.³⁷

Experimental Demonstration of Operational Mode D. By changing the parameters associated with the IA3 region, it is possible to induce dissociation of the mobility-resolved primary fragments (generated from dissociation of a selected ion in IA2). An example, demonstrating the generation of secondary fragment ions (e.g., IMS-IMS-MS operational mode D) is shown in Figure 11. This is a relatively straightforward extension of the split-field approach for fragmenting ions that we described previously.¹⁸ The secondary fragments are generated from the mixture of mobility-resolved primary fragments. It is possible to group the secondary fragments with the appropriate primary fragment precursor because they have coincident D2 drift times.

Figure 11 illustrates example mass spectral slices for dissociation of two different primary fragment ions, the b_6^{2+} [4.78(354.4) \rightarrow 9.83(321.7)] ion and the y_7^{2+} [4.78(354.4) \rightarrow 10.13(404.2)] ion. These mass spectra illustrate that relatively efficient secondary dissociation data can be obtained with signal-to-noise ratios comparable to those of spectra obtained from MS³ experiments. In the two-dimensional representation of the data that is shown, one can see that multiple features are observed at a single m/z value. In the present case, these correspond to the same ions formed either by primary or secondary dissociation. In the present setup, primary dissociation products undergo further mobility separation in D2, whereas secondary fragments are formed at the exit of the drift tube. Secondary fragments have drift times that reflect the original K -selected ion (through D1) and the mobility of the primary fragment ion (through D2). The origin of identical ions can be identified via the notation used to describe them. For example, the peak associated with the b_4 ion produced from dissociation of the primary b_6^{2+} fragment is referenced as 4.78-(354.4) \rightarrow 9.83(321.7) \rightarrow 9.83(408.2). Note that there are two other peaks associated with formation of the b_4 ion at 4.78(354.4) \rightarrow 10.95(408.3) and 4.78(354.4) \rightarrow 11.18(408.3); however, these peaks arise from different primary fragments (as indicated by the nomenclature). The mass spectral slices taken for the b_6^{2+} and y_7^{2+} (Figure 11a,b) demonstrate that the secondary fragmentation data is highly usable. As we have discussed above for IA2 and previously in the original description of a split-field drift tube, fragmentation at IA3 is highly tunable and reproducible.¹⁸

Example IMS-IMS-MS Distributions of Proteins: the $[M + 7H]^{7+}$ Ion from the ESI of Ubiquitin. To this point, we have focused the discussion of IMS-IMS(-MS) analysis on the ability to separate fragment ions from selected precursors. There is, however, another type of experiment that looks very promising,

(38) In addition to references herein, see: Valentine, S. J.; Counterman, A. E.; Clemmer, D. E. *J. Am. Soc. Mass Spectrom.* **1999**, *10*, 1188–1211.

(39) Shevchenko, A.; Wilm, M.; Mann, M. *J. Protein Chem.* **1997**, *16*, 481–490. Taylor, J. A.; Johnson, R. S. *Rapid Commun. Mass Spectrom.* **1997**, *11*, 1067–1075.

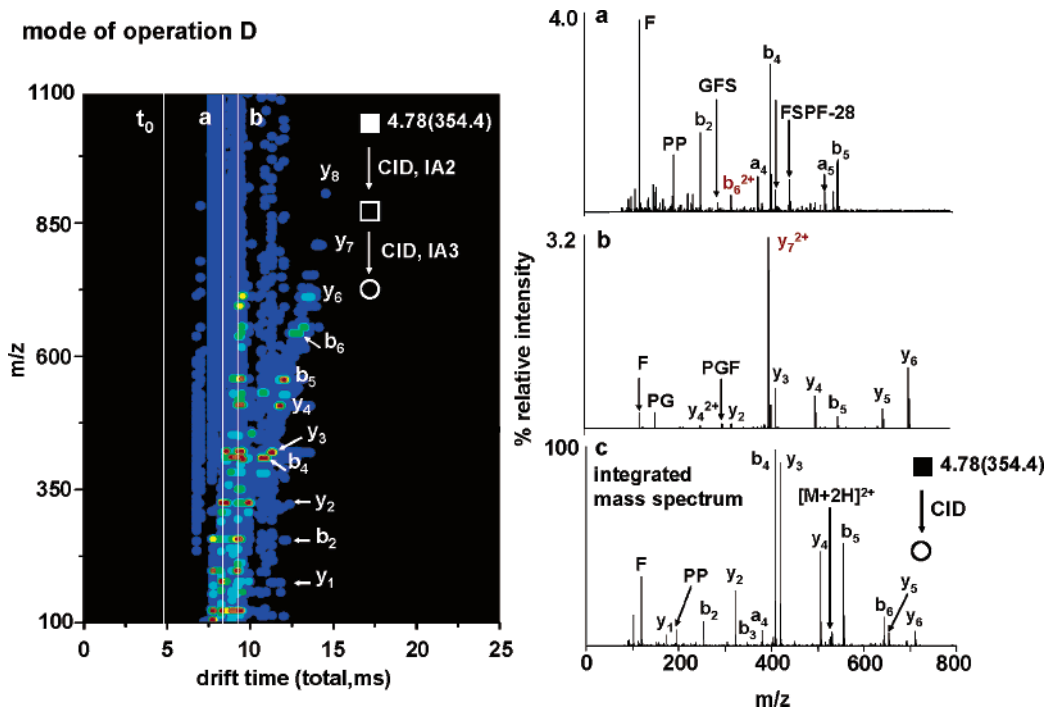


Figure 11. Nested $t_b(m/z)$ distribution obtained for bradykinin ions illustrating operational mode D. Mass spectral slices (obtained by integrating over a narrow drift-time range) showing secondary product ion formation from fragmentation of the primary fragments, b_6^{2+} and y_7^{2+} , are shown in spectra a and b. The spectrum labeled c shows the integrated mass spectrum.

a low-energy activation in which a structural change is induced without inducing fragmentation.

To demonstrate this type of analysis, we have examined ions formed upon ESI of ubiquitin. Ubiquitin is a small protein (76 amino acids) that has been studied by IMS and MS in detail.³¹ Under typical ESI conditions, it is possible to produce a distribution of charge states (from +6 to +13). Mobility measurements show that these charge states exist as a range of different conformations. We have previously described the conformations of different charge states as one of three general types: compact, partially folded, or elongated.⁵ Here, we focus on a distribution of structures for the $[M + 7H]^{7+}$ ion. Figure 12a shows the ion mobility distribution obtained as a drift time slice for this charge state. With no selection or activation, (operational mode A), we observe evidence for the compact and partially-folded states centered at total drift times of ~ 16 and 19 ms, respectively. Interestingly, the higher resolution of the present instrument suggests that we are able to begin resolving different types of compact conformations. Essentially no elongated ions are observed under these conditions ($t_b \sim 23$ ms).

Figure 12b also shows the ability to select a specific conformation (operational mode B). Here, we selected a compact structure. The selection time that was used was deliberately increased slightly beyond the peak maximum for the compact state. Using this setting, we select a conformation that is still very compact, but is slightly larger than those compact ions that make up the majority of the population. The distribution obtained for this selection is remarkable in that the peak is extremely sharp, and there is no evidence that this state is interconverting with other compact forms (something that we have always assumed to be the case).⁵ Instead, it appears that there are many compact structures that cannot be separated in D1, and these many different compact states appear to have stable structures that do

not change significantly during the timescale of the measurement. We are currently investigating this in more detail.

Figure 12 shows two examples of operational mode C. Under the activation conditions employed, we observe no fragmentation of the ubiquitin charge states; however, there are clear structural changes. At ~ 70 V activation, the compact state can be transformed into a new distribution of states (Figure 12c). Some of these may be slightly more compact than the initial structure (similar to the compact states from operational mode A), but a majority appear to be characterized by our partially-folded annotation. Applying ~ 106 V to the IA2 region results in a distribution that favors elongated structures (Figure 12d). In many ways, the activation process and structures that are formed appear to be similar to the results obtained from injected ion studies (upon changing the injection energy),^{31a} however, the ability to initiate structural changes from a specific (selected mobility) geometry has substantial potential for unraveling folding and unfolding pathways as well as the characterization of noncovalent complexes.

Current Capabilities, Limitations, and Some Possible Applications of IMS–IMS Instrumentation. It is worthwhile to consider some figures of merit for the IMS–IMS-MS instrument developed here. We start by considering the total resolving power of this multidimensional separation. Analysis of peaks in the mass spectra shows that the resolution of the reflectron mass analyzer typically ranges from ~ 3500 to 5000.

In theory, the resolution of a drift tube can be calculated from eq 3.²

$$\frac{t}{\Delta t} = \left(\frac{LEze}{16k_B T \ln 2} \right)^{1/2} \quad (3)$$

In practice, resolving powers for biological ions are typically much less than theory (because many unresolved configurations or

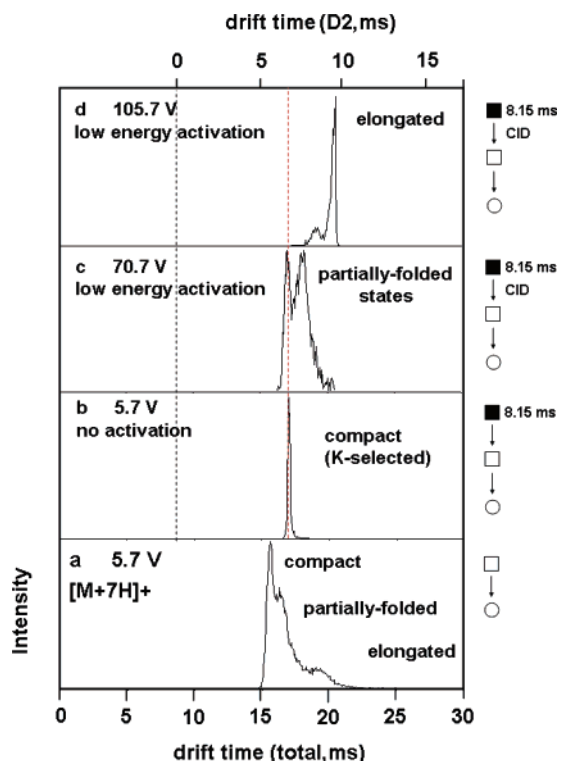


Figure 12. Drift time slices of the $[M + 7H]^{7+}$ of ubiquitin from IMS-IMS-MS experiments: (a) The ion mobility distribution, obtained in operation mode A, indicates the presence of compact, partially-folded, and elongated structures. (b) A compact state has been selected at G2 ($t_{D1} = 8.15$ ms, $50 \mu\text{s}$) from the total distribution of structures for this charge state in operational mode B. (c) Upon low-energy activation of the compact structure in IA2 (operational mode C), a portion of the selected ion distribution unfolds to several partially-folded states and even more compact structures (indicated by the distribution to the left of the red line). (d) At higher energy in operational mode C, the selected distribution is almost completely converted to an elongated structure. Note that the elongated structure in (d) has a shorter drift time than in (a) because it was produced in IA2.

structures that interconvert inside the drift tube may exist). Over the course of developing this instrument, we have recorded $t/\Delta t_{\text{whm}}$ ($D1 + D2$) values as high as ~ 150 . Typically, values range from ~ 80 to 120 . Analysis of peaks from D2 separations typically yields values from 40 to 70 .

It is interesting to consider the IMS-IMS-MS peak capacity. One of the long-standing limitations of IMS-MS measurements is that IMS and MS are not orthogonal separations. That is, ions of higher mass are greater in size (or collision cross section). Because of this, peaks in IMS-MS data usually fall along lines. For example, small peptides (~ 10 residues) typically vary over a range of $\sim 20\%$. If we assume a resolving power of 50 in D1, this means that within a specified m/z range, only ~ 10 peaks would be resolved. Thus, we estimate the total IMS-MS peak capacity to be about an order of magnitude greater than the capacity of the mass spectrometer above.

The ability to produce fragments (especially from multiply-charged ions) creates a more interesting situation. In this case of complete fragmentation and separation by D2, the original precursor ion mobility is no longer correlated with fragment masses that are formed. In this case, we estimate the total peak capacity to be ~ 500 (the full factor of 50 for D1 separation and

the factor of 10 for D2). In practice, fragments are also resolved on the basis of differences in charge states such that the total peak capacity is somewhat greater.

There are several caveats associated with these ideas. First, we note that, of course, once formed, fragment ion mobilities and masses will be correlated with one another (in the D2 instrument). Thus, we estimate a gain of only an additional order of magnitude from D2. The resolving power of D1 increases because the correlation of mobility and mass is removed upon dissociation. Second, we note that this peak capacity is not fully realized at this time because we operate the instrument in a selected ion mode (analogous to an MS1 selection mode). Thus, only a single ion is examined at one time. We are currently developing an IMS-IMS instrument in which the second IMS region is much shorter than the first, with the aim of operating IMS-IMS experiments in a nested mode such that all ions can be examined.

Perhaps the most interesting aspect of IMS-IMS is that it is possible to induce structural changes (either to produce different conformations or fragment ions) at a single point inside the drift tube. This is analogous in many ways to the ability to activate a m/z -selected ion by MS-MS techniques. However, unlike MS techniques, the second IMS separation is sensitive to structural differences. Thus, in some cases, isomers (that also have identical mobilities and would not be resolved by either MS or IMS alone) may be resolved in the second IMS analysis (either as a precursor with a different mobility upon activation or as a fragment ion with a different structure).

SUMMARY

In this paper, we have described the development of the first IMS-IMS instrument. The approach utilizes successive stages of IMS separation that are connected with ion funnels. The use of ion funnels dramatically improves transmission in these systems by radially focusing diffuse ion clouds. IMS-IMS has similarities with MS-MS methods. Unlike isolation of a specific m/z ion by MS, the use of IMS allows ions of specific mobility to be selected. This should prove to be a powerful separation because it should be possible to accumulate concentrated pulses of even relatively weak signals for further study with other techniques.

Second, we have shown that it is possible to induce dissociation of a mobility-selected ion inside the instrument to create distributions of fragments. These fragment ions can be separated again in the second drift tube prior to m/z analysis. The combined mobility and m/z dispersion of fragments already has yielded an interesting result. In the case of bradykinin, b-type fragment ions appear to exist as two stable conformations that can be resolved in the drift tube.

Third, we have shown that by exposing the mobility-resolved fragments of a selected ion to energizing collisions, it is possible to create secondary fragment ions. This technique is effectively a means of generating secondary fragments for distributions of primary fragment ions in a parallel fashion and is analogous in many ways to the well-known MS-MS-MS method.

Finally, we have shown that it is possible to select a specific conformation from the first IMS separation and collisionally activate (but not fragment) to generate a new distribution of conformations. We demonstrated this type of experiment by examining the $+7$ charge state of ubiquitin. In this system, we selected a compact conformation and activated it to form a

distribution of more elongated structures. This experiment has many similarities to the injected ion drift tube experiments that have yielded a substantial amount of information about the gas-phase structures of proteins and peptides.

ACKNOWLEDGMENT

This work is supported by grants from the National Science Foundation (CHE-0078737), the National Institutes of Health (AG-024547-01 and P41-RR018942), the Indiana 21st Century Research and Technology Fund, and funding in part from the METACyt initiative funded by a grant from the Lilly Endowment. The PNNL work was supported by Laboratory Directed Research and

Development Program and the NIH National Center for Research Resources (RR 18522). Pacific Northwest National Laboratory is operated by the Battelle Memorial Institute for the U.S. Department of Energy through contract DE-AC05-76RLO1830. We are grateful for many stimulating conversations with Andy Alexander, John Poehlman, and C. Ray Sporleder, as well as other reviewers of our manuscripts who continue to encourage us to improve these techniques.

Received for review June 15, 2005. Accepted March 27, 2006.

AC051060W